Generated using the official AMS LATEX template v5.0

Top-of-atmosphere albedo bias from neglecting three-dimensional cloud radiative effects

Clare E. Singer*, Ignacio Lopez-Gomez, Xiyue Zhang†

Department of Environmental Science and Engineering, California Institute of Technology

Tapio Schneider

Department of Environmental Science and Engineering, California Institute of Technology, and Jet Propulsion Laboratory, California Institute of Technology

**Corresponding author*: Clare E. Singer, csinger@caltech.edu

†Current affiliation: Department of Earth and Planetary Sciences, Johns Hopkins University, Baltimore, MD, USA.

ABSTRACT

Clouds cover on average nearly 70% of Earth's surface and regulate the global albedo. The magnitude of the shortwave reflection by clouds depends on their location, optical properties, and three-dimensional (3D) structure. Due to computational limitations, Earth system models are unable to perform 3D radiative transfer calculations. Instead they make assumptions, including the independent column approximation (ICA), that neglect effects of 3D cloud morphology on albedo. We show how the resulting radiative flux bias (ICA-3D) depends on cloud morphology and solar zenith angle. Using large-eddy simulations to produce 3D cloud fields, a Monte Carlo code for 3D radiative transfer, and observations of cloud climatology, we estimate the effect of this flux bias on global climate. The flux bias is largest at small zenith angles and for deeper clouds, while the negative albedo bias is most prominent for large zenith angles. In the tropics, the radiative flux bias from neglecting 3D radiative transfer is estimated to be 4.0 ± 2.4 W m^{-2} in the mean and locally as large as 9 W m^{-2}.

1. Introduction

Earth's average albedo is roughly 29%, with clouds accounting for about half of the reflection of solar radiative energy fluxes back to space (Stephens et al. 2015). Accurately simulating clouds is crucial for modeling Earth's albedo. However, Earth system models (ESMs) struggle to accurately represent the albedo's magnitude, spatial patterns, and seasonal variability (Bender et al. 2006; Voigt et al. 2013; Engström et al. 2015). Simulating clouds is difficult for several reasons, but one major factor is their wide range of spatial scales. Clouds have complex three-dimensional (3D) morphologies created by turbulent motions at length scales down to tens of meters or smaller. However, the typical resolution of an ESM is around only 10–100 km in the horizontal and 100–200 m in the vertical in the lower troposphere (Schneider et al. 2017). This discrepancy means that clouds are not explicitly resolved in ESMs. Instead, they are represented by parameterizations and, for purposes of radiative transfer (RT) calculations, are approximated as broken plane-parallel structures within grid cells (Marshak and Davis 2005).

The plane-parallel approximation (PPA) leads to important biases in RT calculations due to the nonlinear relation between optical depth and albedo (Cahalan and Wiscombe 1992). Over the past 20 years, RT solvers have made significant progress in the reduction of these biases, either by making use of semi-empirical deterministic parameterizations of cloud heterogeneity (Shonk and Hogan 2008) or through stochastic sampling of possible cloud states across different spectral intervals (Pincus et al. 2003). These approximate solvers are likely to become even more accurate in the future, as dynamical parameterizations provide increasingly detailed cloud statistics (e.g., Cohen et al. 2020). Moreover, the PPA may possibly be avoided in ESMs by using embedded cloud-resolving models (Kooperman et al. 2016), an approach known as cloud superparameterization (Khairoutdinov and Randall 2001).

This progress has led to renewed interest in another source of bias that was, until recently, shadowed by biases due to the PPA: the treatment of horizontal radiative fluxes in ESMs (Cahalan et al. 1994; Schäfer et al. 2016; Hogan et al. 2019). ESMs make the independent column approximation (ICA) when performing RT calculations. This approximation neglects horizontal radiative fluxes between neighboring grid cells, decoupling the RT calculation between atmospheric columns to make the problem computationally tractable. 3D radiative transfer will remain too expensive to run in ESMs in the foreseeable future, making the ICA a necessary simplification (Hogan and Bozzo 2018). For this reason, it is important to quantify and document the albedo bias due to the ICA.

In this context, the effect of cloud structure on horizontal radiative transfer has gained attention, enabled by advances in computation that make 3D RT feasible at high spectral resolution and over large domains (Mayer and Kylling 2005; Emde et al. 2016; Villefranque et al. 2019; Gristey et al. 2019; Veerman et al. 2020). The structural differences between ICA and a full 3D RT calculation have been documented before (Barker et al. 2003; Marshak et al. 1995b; Barker et al. 2012), and many alternatives to ICA have been proposed to minimize their mismatch (e.g., Marshak et al. 1995a; Várnai and Davies 1999; Frame et al. 2009; Hogan and Shonk 2013; Wissmeier et al. 2013; Okata et al. 2017; Hogan et al. 2019). Nevertheless, most studies have been focused on theoretical cases, small spatial and temporal domains, or improving satellite retrieval algorithms. Some notable exceptions are Cole et al. (2005) and Barker et al. (2015), who compared 2D/3D and ICA RT calculations to estimate the bias present in ESMs using a superparameterized cloud resolving model and coarse-resolution, two-dimensional cloud fields retrieved from CloudSAT and CALIPSO, respectively.

Here we discuss the magnitude of the bias that results from neglecting the 3D cloud radiative effects by making the ICA. We use large-eddy simulations (LES) to generate 3D cloud fields representing three canonical cloud regimes: shallow convection, stratocumulus, and deep convection.

These cloud regimes are representative of the clouds typically found in the tropics. Then we calculate the bias between the true reflected flux and the flux approximated by ICA using a Monte Carlo RT code. The radiative flux bias is shown to vary with zenith angle and cloud type. Because the zenith angle varies with the diurnal and seasonal cycle, we quantify the effect of the 3D bias on these timescales. Finally, using global satellite observations of cloud climatology, we estimate the spatiotemporal bias that would result in global models that resolve clouds but still make the ICA. As stated earlier, most ESMs make the ICA and use some cloud heterogeneity parameterization to reduce the PPA bias, so the bias associated with only the ICA is an underestimate of the total bias. Because of the diversity of assumptions made by global models to account for phenomena such as cloud overlap, and the fundamental resolution dependence of cloud heterogeneity emulators, in this study we focus on the bias resulting from RT using only the ICA on fully resolved 3D cloud structures from LES.

2. Methods

a. Large-eddy simulations of clouds

We generate three-dimensional cloud fields from high-resolution LES using the anelastic solver PyCLES (Pressel et al. 2015, 2017). The LES are run in three dynamical regimes to simulate shallow cumulus (ShCu), stratocumulus (Sc), and deep-convective clouds (Cb); details can be found in appendix A. ShCu clouds are convective clouds with typical cloud cover of 10–20% and cloud top height (CTH) around 2 km. They occur frequently over low- and mid-latitude oceans. In this study, ShCu are represented by two LES case studies, BOMEX and RICO, which represent non-precipitating and precipitating convection over tropical oceans, respectively (Siebesma et al. 2003; vanZanten et al. 2011). Sc clouds are shallow, with CTH only around 1 km. They have near

100% cloud cover and typically blanket subtropical oceans off the west coast of continents. Sc are represented by the DYCOMS-II RF01 LES case of a Sc deck off the coast of California (Stevens et al. 2005). Cb clouds are deep convective thunderstorm clouds that occur frequently over mid-latitude continents in summer and in the tropics, e.g., in the intertropical convergence zone (ITCZ). Their CTH can reach up to 15 km or higher, they often contain ice, and anvils at the top contribute to a cloud cover around 30%. Cb clouds are represented in this paper by the TRMM-LBA LES case, based on measurements of convection over land in the Amazon (Grabowski et al. 2006).

An ensemble of snapshots is used to estimate the mean and variance of the bias for each cloud type. For ShCu and Sc, we take snapshots evenly spaced in time starting once the simulation has reached a statistically quasi-steady state, after an initial spin-up period. The snapshots are chosen to be at least one convective turnover time apart (1 hour for BOMEX and RICO, 30 minutes for DYCOMS-II RF01, and 90 minutes for TRMM-LBA). For the Cb case we take snapshots from an initial-condition ensemble at several time points representative of transient and fully-developed deep convection at 4, 5.5, and 7 hours into the simulation (10:00, 11:30, and 13:00 local time). We also include snapshots from an initial-condition ensemble run over a larger domain (40 km, compared to the original 20 km) to capture a higher degree of convective aggregation (Jeevanjee and Romps 2013; Wing et al. 2017; Patrizio and Randall 2019). We use only the snapshots at 13:00 local time of fully-developed deep convection, characterized by stable liquid and ice water paths, for the idealized calculations, and then we use all time points to make our best estimate of the global flux bias. We choose ensemble sizes that capture the natural variability of morphology in each LES case: 10 for ShCu (BOMEX and RICO, 10 each), and 5 for Sc (DYCOMS-II RF01); for Cb we take 15 snapshots from each time point (45 in total) from the 20 km TRMM-LBA simulations and 5 snapshots of fully-developed, more aggregated deep convection from the 40 km

TRMM-LBA agg. simulations. The smaller ensemble is determined to sufficiently capture the dynamical variability for the larger domain.

The increase in convective aggregation for the larger domain simulations can be seen in typical measures such as the variance of the column relative humidity or total precipitable water (Wing et al. 2017) (see appendix A, Fig. A1). The domain-mean cloud cover, cloud top height, and cloud water path from these two sets of simulations are similar, indicating that the difference in radiative flux bias is not being driven by a change in the mean cloud state. Although we see more aggregation in the larger-domain, we expect that an even larger simulation domain would yield more convective aggregation (Patrizio and Randall 2019); however, due to computational limitations, we do not consider larger domains. Furthermore, for larger scales, consideration of synoptic noise may become important and disrupt the self-aggregation of convection. The ShCu results are unchanged (not shown) for larger domain sizes, because the dynamics have already converged for the sufficiently large domains used. Although we do see an expected reduction in variance across the ensemble ($N_{\mathrm{LES}} = 10$) which is expected due to the larger dynamical variability captured in each snapshot of the larger domain.

b. Radiative transfer computations

The RT calculations were done using the libRadtran software package with the MYSTIC Monte Carlo solver (Mayer and Kylling 2005; Mayer 2009; Emde et al. 2016). The MYSTIC solver requires 3D fields of liquid and ice water content and particle effective radius as input. We use MYSTIC to do the full 3D RT and we turn on the `mc_ipa` setting to do the ICA calculations. The LES uses bulk microphysics schemes (2-moment for liquid, 1-moment for ice) and does not explicitly compute the effective radius. To compute the effective radius, we follow the parameterization from Ackerman et al. (2009) and Blossey et al. (2013) for liquid and Wyser (1998) for ice (appendix

B). For the RT calculation, MYSTIC computes the scattering phase function. In the case of liquid droplets, which can be assumed spherical, the full Mie phase function is used. For the case of ice clouds, a parameterization of the habit-dependent scattering must be used. We find that the results are insensitive to the choice of ice parameterization (Fig. B1) because the reflected flux signal is dominated by the liquid droplets for the clouds simulated.

c. Observations of cloud climatology

The LES cloud fields allow for precise calculation of the 3D cloud radiative effect on small domains. To estimate the global impact of the 3D cloud radiative effect, we use the results from LES along with satellite observations of cloud climatology and surface albedo to extrapolate from these few cases to a global picture. We find that cloud top height (CTH) is a simple, but robust, predictor of the flux bias. We use the International Satellite Cloud Climatology Project (ISCCP) D2 dataset of cloud top height (Rossow et al. 1999; Rossow and Duenas 2004; Marchand et al. 2010; Stubenrauch et al. 2012, 2013). The ISCCP D2 cloud product is a monthly climatological mean with spatial resolution of $1^\circ \times 1^\circ$ constructed from measurements during the period 1984–2007. These data are collected by a suite of weather satellites that are combined into a 3-hourly global gridded product at the D1 level and averaged, including a mean diurnal cycle, into the D2 product we use.

We also account for the observed surface albedo that varies seasonally and spatially and affects the flux bias. We use observations of surface albedo from the Global Energy and Water Exchanges Project's surface radiation budget product version 3.0, which is aggregated to a monthly mean climatology for the period 1984–2007 and gridded to $1^\circ \times 1^\circ$.

3. Radiative flux bias dependence on zenith angle

The top-of-atmosphere (TOA) radiative flux bias is measured (in W m^{-2}) as the difference in reflected irradiance between the ICA and 3D RT calculations. A positive bias means that the ICA is reflecting more energy than the 3D truth, and the Earth system is artificially dimmed. The albedo bias ($\Delta\alpha$) is computed as the flux bias ($\Delta F = F_{\mathrm{ICA}} - F_{\mathrm{3D}}$) divided by the total incoming solar flux (F_{in}),

$$\Delta\alpha = \frac{\Delta F}{F_{\mathrm{in}}} \times 100\%. \tag{1}$$

Fig. 1 shows the flux and albedo biases (ICA−3D) for the five cases of ShCu, Sc, and Cb clouds. The solid lines show the ensemble mean bias and the shading denotes the combined variance (σ^2) of the ensemble,

$$\sigma^2 = \frac{1}{N_{LES}} \sum_{i=1}^{N_{\mathrm{LES}}} \left[\left(\sigma_{i,\mathrm{ICA}}^2 + \sigma_{i,\mathrm{3D}}^2 \right) + \left(\Delta F_i - \langle \Delta F \rangle \right)^2 \right] \tag{2}$$

where N_{LES} is the number of ensemble members, $\sigma_{i,\mathrm{ICA}}$ and $\sigma_{i,\mathrm{3D}}$ are the standard deviations from the MYSTIC solver photon tracing, ΔF_i is the flux bias of each ensemble member, and $\langle\cdot\rangle$ denotes a mean over the LES ensemble. This variance includes both the statistical noise from the Monte Carlo RT and the dynamical variability of the cloud field (which are assumed uncorrelated). The Monte Carlo noise is proportional to $\frac{1}{\sqrt{n}}$ where $n = 10^4$ is the number of photons used for the RT simulation, or about 1% for these calculations. The variance between cloud scenes is much larger than the Monte Carlo error, by more than an order of magnitude.

Sc show negligible deviation between ICA and 3D reflected fluxes. For convective clouds (ShCu and Cb), the bias from the ICA is positive, except for ShCu at very large solar zenith angles. At large zenith angles, ShCu show a large negative flux and albedo bias for ICA. ShCu scatter far fewer photons than Cb due to the low cloud cover and their small vertical extent (1–2 km). Cb exhibit the largest reflected irradiance and also the largest bias between the ICA and 3D RT calculations. While the mean flux bias is similar, the structure of the bias with zenith angle is markedly different for the two domain sizes (Fig. 1). For the small-domain simulations with a lesser degree of aggregation, the bias is approximately linear with zenith angle. For the more aggregated case, the flux bias is nearly uniform up until a zenith angle of 60° and then decreases rapidly towards zero; this translates to an albedo bias that peaks at large zenith angles (around 70°).

The convective clouds show much more variation than the stratiform clouds between snapshots due to the variability in cloud cover even in a statistically steady state. The less aggregated Cb clouds have the largest variability, which is expected since the domain size is small relative to the scale of the clouds, i.e., in each snapshot we capture only approximately one deep convective cloud, compared to many small cumulus clouds; therefore, we are effectively averaging over fewer realizations even though we take our ensemble size to be larger. Similarly, for the more aggregated Cb clouds, since we use a four times larger domain, a smaller ensemble ($N_{\mathrm{LES}} = 5$ compared to 15) is large enough to capture the variability.

In the ICA, the horizontal photon fluxes between neighboring columns are ignored. For the Sc clouds that uniformly cover the whole domain (Fig. 2c), this assumption has little effect: the flux bias is near zero for all zenith angles. However, for cumulus clouds, the ICA has two effects that are described in detail by Hogan et al. (2019). 1) The long-recognized effect that is present during 3D radiative transfer of "cloud-side illumination." This describes how when horizontal photon fluxes are permitted, the photons can encounter the side of a cloud and be scattered by it. This effect acts to enhance cloud reflectance in 3D, and thus would appear as a negative flux bias in our terminology. 2) The newer effect that Hogan et al. (2019) present is of "entrapment." This mechanism is similar to the "upward trapping" mechanism discussed by Várnai and Davies (1999). It describes how in 3D a scattered photon may be intercepted by another cloud, or the same cloud, higher in the domain and scattered back down to the surface. In the ICA by contrast, when a photon travels through clear-sky and is scattered by a cloud, it will necessarily travel back through the same column of clear-sky to the TOA. The entrapment mechanism acts to decrease cloud reflectance in 3D, i.e., it creates a positive flux bias. The calculated 3D effects we show in Fig. 1 are a combination of these competing mechanisms.

For small zenith angles, when the sun is overhead, the convective clouds (ShCu and Cb) produce a positive flux bias because entrapment is dominant over cloud-side illumination. For large zenith angles, the flux and albedo bias from ShCu is negative because cloud-side illumination becomes the dominant effect. In the mean, the zenith angle at which the flux bias becomes negative is around 70°, but for the individual ensemble members this ranges from around 45° to 75°. This has been seen before for ShCu by Barker et al. (2015) and Hogan et al. (2019). For Cb clouds, however, even at large zenith angles, the flux and albedo biases remain positive, indicating that the entrapment mechanism continues to dominate over cloud-side illumination. This is not the case for every scene in the Cb ensemble, but it is true in the mean, in agreement with the results from Hogan et al. (2019). This difference between ShCu and Cb is related to the aspect ratio of the clouds; the cloud-side illumination mechanism can only become dominant if the aspect ratio is close to one. Furthermore, in the case of the more aggregated Cb clouds, a greater degree of aggregation decreases the surface area to volume ratio of the clouds, or what Schäfer et al. (2016) call the length of cloud edge or "cloud perimeter." A smaller cloud perimeter will decrease the cloud side illumination as well as the entrapment efficiency of the cloud (Hogan et al. 2019). The uncertainty in flux bias due to the degree of aggregation of deep convection is much larger than the spread across the LES ensembles and represents a structural error which is more challenging to quantify.

These 3D cloud effects can be understood from Fig. 2, which shows illustrations of the clouds from the four LES cases. The scattered shallow cumulus in the BOMEX and RICO cases have aspect ratios near one, which allows for cloud-side illumination at large zenith angles to dominate over the entrapment mechanism. The DYCOMS-II RF01 stratocumulus clouds are quite homogeneous over this small domain, therefore, ICA biases are small. As discussed in Hogan et al. (2019), when in-cloud heterogeneity is larger, the entrapment effect is larger. Finally, for the deep TRMM-LBA clouds, the entrapment mechanism remains dominant even for large zenith angles because the clouds at higher levels can intercept and trap outgoing photons that are able to escape to TOA in the ICA.

In addition to the LES ensembles described previously, we run one additional set of tests to quantify the dependence of the flux bias calculations on the LES resolution (Fig. 3). We take the original LES simulations and systematically coarse-grain the 3D fields to lower resolution. Doing so ensures that we do not change the dynamics of the clouds so that we can test the effect of resolution on only the radiative transfer. We are not able to bridge the gap all the way to ESM scales (10–100 km horizontal resolutions) due to computational limits on running the LES, but we show results across a range of horizontal scales. When coarse-graining, we keep the vertical resolution fixed to better represent the very large aspect ratio grid boxes found in ESMs compared to the relatively isotropic grid boxes in LES. The mean TOA flux bias is nearly constant across resolutions for the shallow clouds (Sc and ShCu). For Cb, the mean TOA flux bias decreases with larger grid spacing, as expected, from around 17 W m^{-2} at the original resolution and down to 6 W m^{-2} for 2 km horizontal resolution. Since the bias does not asymptote towards smaller horizontal grid spacing, we conclude that our estimated bias is a lower bound in this regard, and we expect that if the LES could be run at higher resolutions we would find an even larger bias between the ICA and 3D.

4. Seasonal cycle of radiative flux bias

To assess the climate impact of the radiation bias resulting from the ICA, we consider the flux and albedo bias for each cloud type as a function of day of year and latitude. This calculation is done by assuming that the LES-generated cloud field is present at any given latitude circle on any given day of the year. This exercise is done not to be realistic, but to demonstrate the impact each cloud type might have on Earth given the spatiotemporal variations of solar zenith angle. For any location and time, including a diurnal cycle, the solar zenith angle is calculated and the flux bias is estimated based on the results presented in Fig. 1. The flux and albedo biases are computed hourly and averaged to show the daily-mean bias.

Fig. 4 shows the annual mean and seasonal cycle of TOA flux and albedo biases for each cloud type. Note that the color scale varies for each cloud type. To estimate the uncertainties of the annual mean bias, we calculate the LES ensemble spread as follows. For each hour in the year and each latitude, the solar zenith angle is calculated, and we interpolate between integer zenith angles to find the flux bias. This is done individually for each LES cloud scene in the ensemble. The ensemble mean for each latitude and day of the year is shown (colored contour plots in Fig. 4) as well as the annual mean of the ensemble (black lines on Fig. 4). The spread across the ensemble in the annual mean is shown as one standard deviation (gray shading on Fig. 4).

All cloud types show zero flux bias in regions of polar night where there is no incoming solar flux. Both ShCu cases show similar patterns of flux bias with latitude and time (Fig. 4a and c). As seen in Fig. 1, these cases both have a negative bias for high solar zenith angles ($> 70°$), and therefore the net flux (and albedo) bias during the shoulder seasons at very high latitudes is negative. At lower latitudes, where the diurnally averaged zenith angle is never larger than $70°$, the net flux bias is always positive. Sc show a very small flux (and albedo) bias for all zenith angles due to their high cloud cover and optical depth, but they do exhibit a small positive flux bias (~ 0.5 W m^{-2}) during summer in high latitudes (Fig. 4e). For Cb, the flux bias is comparatively large and always positive (Fig. 1). In the less aggregated state, the flux bias is nearly linear in zenith angle which gives rise to a bias pattern that roughly mimics the insolation pattern with latitude and day of year (Fig. 4g). In the more aggregated state, the flux bias is nearly constant across most zenith angles, but actually has a slight peak near 60°, which results in a bias that peaks during the polar summers (Fig. 4i). The albedo bias for Cb is largest and positive in the high-latitudes during summer, though more strongly so for the more aggregated convection (Fig. 4h and j). While slightly counter-intuitive, this is simply because we are calculating the 24-hour daily mean bias, so at lower latitudes we include the zero bias nighttime periods which are minimal in polar summers.

In addition to the diurnal bias that arises from changes in zenith angle from sunrise to sunset over the course of the day, there is a seasonal cycle in the radiation bias resulting from Earth's orbital obliquity. For instance, equatorial deep convective clouds create a TOA albedo bias that peaks during northern hemisphere summer and has a minimum in winter (Fig. 4h and j).

5. Implications for Climate Models

To make an assessment of the effect that the 3D radiative transfer through cloud fields has on climate simulated with ESMs, we must account for the climatological occurrence of different cloud types in space and time. A simple parameter that can account for much of the flux bias variability is cloud top height (CTH), defined as the 90th percentile height observed in the LES domain to exclude small, ephemeral clouds at the domain top. By regressing the flux bias against CTH for 91 evenly spaced solar zenith angles between 0 and 90°, constraining the regression lines to pass through the origin because there is no flux bias in clear-sky conditions (CTH = 0), we observe a robust positive correlation between CTH and flux bias (Fig. 5). The best fit line and confidence intervals are estimated with Gaussian Process regression; we use a dot product kernel, with the intercept constrained to zero, and a constant nugget that is optimized via a grid-search to match the empirically calculated sample variance within 2 km bins of CTH. The positive correlation between CTH and flux bias, though not perfect, allows us to approximate TOA flux biases using CTH on the global scale. We choose CTH as our proxy for flux bias because it is robustly observed by satellite and, of the other cloud properties we explored, the best predictor for flux bias (Fig. C1). Despite the fact that the radiative flux bias certainly depends on more than just CTH, we use it here as a first approximation to model the flux bias.

Using this relationship between CTH and flux bias for a series of zenith angles, we can use the observed climatological CTHs from ISCCP to infer the resulting flux bias that would be associated with using the ICA for RT calculations in place of 3D RT. The monthly temporal resolution is not inherently an issue for this analysis given that the relationship we use between CTH and flux bias is linear.

Additionally, we may account for the variations in surface albedo. In the RT calculations, we assume a constant surface albedo of the ocean $\alpha_O = 0.06$. The surface albedo (α_s) affects the computed flux and albedo biases: in the extreme, if $\alpha_s = 1$ then there will be no bias from the clouds because all photons will be reflected to the TOA by the surface. The total scene albedo stems from scattering by the clouds and scattering by the surface. This depends on the surface albedo, the cloud albedo (α_c), and the cloud fraction (f_c). If we ignore multiple-scattering, the total scene albedo is

$$\begin{aligned} \alpha &= f_c\alpha_c + (1 - f_c)\alpha_s + f_c(1-\alpha_c)\alpha_s \\ &= \alpha_s + f_c(1-\alpha_s)\alpha_c. \end{aligned} \tag{3}$$

The first term comes from reflection from the clouds, the second from reflection by the surface below clear-sky, and the third from reflection from surface below clouds. The albedo bias is,

$$\Delta\alpha = f_c(1-\alpha_s)\Delta\alpha_c \tag{4}$$

where $\Delta\alpha = \alpha_{\mathrm{ICA}} - \alpha_{\mathrm{3D}}$. Therefore, the albedo bias (and flux bias) scale with $(1-\alpha_s)$, so we can correct for the effect of surface albedo by multiplying our computed flux or albedo bias by the ratio of the surface absorptions:

$$\Delta\alpha|_{\alpha_s} = \left(\frac{1-\alpha_s}{1-\alpha_O}\right)\Delta\alpha|_{\alpha_O}. \tag{5}$$

See appendix C for justification of this assumption (Fig. C2).

To construct the annual-mean flux bias map shown in Fig. 6, we first calculate the solar zenith angle for each location on Earth and each hour of the year. Then, we obtain the flux bias given the observed CTH from the linear regression at the given zenith angle (Fig. 5). Finally, we make a correction using Eq. 5, based on the ratio of the observed surface absorption to the assumed ocean surface absorption used in the MYSTIC RT calculations. This flux bias is an estimate of the bias that would be present in an ESM which is able to resolve the relevant dynamical scales for clouds, but makes the ICA during radiative transfer. This bias is smaller than the bias present in current ESMs, which must also correct the biases due to PPA using parameterizations, given their very coarse horizontal resolution.

We focus on the tropics (30°S to 30°N, red box on Fig. 6), where our estimation of flux bias based on the 4 LES cases is most robust and relevant; for higher-latitudes, we do not necessarily capture all the relevant cloud regimes with our sample of LES clouds, and therefore do not claim to make a rigorous estimate of the flux bias. Shown in the left inset plot is the zonal-mean flux bias. The shading represents 1σ error from the linear regression of flux bias on CTH shown in Fig. 5 (as opposed to spatial or temporal variability).

The largest bias occurs over the tropics in the ITCZ region (Fig. 6). It corresponds to locations where the tallest clouds on Earth exist and where the mean zenith angle is smallest. The region of maximum bias migrates seasonally following the location of the ITCZ (and maximum insolation). Seasonal variations in cloud cover and cloud type are also manifest in the seasonal cycle of the 3D flux bias. In the annual mean, the zonal-mean tropical flux bias is estimated to be 4.0 ± 2.4 W m^{-2}, and the maximum flux bias is around 9 W m^{-2}. The annual-mean, zonal-mean tropical albedo bias is $0.8 \pm 0.5\%$.

Our results are of the same order as those reported in Cole et al. (2005), who employ 2D radiative transfer calculations in a superparameterized ESM with 4 km horizontal resolution, sufficient to partially resolve deep convective clouds which explain the majority of the global flux bias. They also found the largest flux bias occurring over the ITCZ region, with a maximum bias of 5 W m^{-2} and tropical zonal-average bias of 1.5 W m^{-2}.

6. Summary and conclusions

In this paper we estimate the TOA flux and albedo biases that result from neglecting 3D radiative transfer through cloudy atmospheres. Although TOA radiative biases in current ESMs are predominantly due to deficiencies of subgrid-scale dynamical parameterizations that generate cloud cover biases, as convection parameterizations improve and model resolution increases, the relative contribution of 3D radiative effects to the total model error will increase. We quantify the radiative flux and albedo bias that results from making the ICA by using a 3D Monte Carlo radiative transfer scheme applied to LES-generated cloud fields. The flux and albedo biases are assessed across different cloud regimes and solar zenith angles. We take our findings from the four canonical LES cases and apply them to observed climatological cloud occurrence to infer the spatially- and temporally-resolved flux and albedo biases.

Previous studies of the 3D effects of clouds have focused primarily on shallow cumulus clouds, but we find that the largest bias comes from deep convective clouds. The flux bias is large and positive for deep convective clouds at small zenith angles and the albedo bias is large and negative for shallow cumulus clouds at large zenith angles. These results quantitatively agree with previous studies using LES clouds to assess 3D effects (Hogan et al. 2019). There is room for future work considering a larger ensemble of cloud morphologies, which could be generated again by LES or alternatively could be retrieved from satellite observations. Our inferred global flux bias is based on only four tropical/subtropical LES cases and therefore does not represent the full diversity of cloud morphologies. This methodology cannot fully capture the effects of mid-latitude storms, for instance, which is why we do not emphasize our results outside of the tropics.

We use the observed correlation between cloud top height and TOA flux bias from our LES ensemble to estimate the global spatiotemporal bias from neglecting 3D radiative transfer in a high-resolution ESM. We choose a simple linear model to map from satellite observations of climatological cloud top heights to TOA flux bias. The deviations in our regression fit suggest that there is potential for a more robust mapping from cloud properties to radiative flux bias. Future work is necessary to explore this path towards a parameterization of 3D radiative effects in ESMs.

The large flux bias for Cb clouds at small zenith angles translates into a seasonal bias that peaks just off the equator in the summer hemisphere, tracking the position of the ITCZ. We estimate the annual-mean tropical-mean flux bias to be 4.0 ± 2.4 W m^{-2}. The flux bias computed here is small compared to the TOA shortwave flux RMS error typical for CMIP5 and CMIP6 models, which is on the order of 10 W m^{-2} (Zhao et al. 2018; Hourdin et al. 2020). However, the 3D bias is still comparable to the signal of anthropogenic greenhouse gas emissions for the coming decades, which is on the order of 2.5–3.1 W m^{-2} (Myhre et al. 2013). These results highlight the importance of considering the 3D radiative fluxes through clouds for Earth's radiation budget and Earth system modeling.

Acknowledgments. C.E.S. acknowledges support from NSF Graduate Research Fellowship under Grant No. DGE-1745301. I.L. is supported by a fellowship from the Resnick Sustainability Institute at Caltech. This research was additionally supported by the generosity of Eric and Wendy Schmidt by recommendation of the Schmidt Futures program and the Hopewell Fund. Part of this research was carried out at the Jet Propulsion Laboratory, California Institute of Technology, under a contract with the National Aeronautics and Space Administration.

Data availability statement. All code or data used in this paper are freely available online. The LES were run using the PyCLES code (`https://climate-dynamics.org/software/#pycles`). The radiative transfer computations were done using the libRadtran code (`http://www.libradtran.org`). Post-processed LES 3D fields used as input files for libRadtran computations are available in Singer et al. (2020). The ISCCP data were downloaded from `https://climserv.ipsl.polytechnique.fr/gewexca/` and the GEWEX albedo measurements were downloaded from `https://eosweb.larc.nasa.gov`.

APPENDIX A

LES model setup

LES are performed using the anelastic fluid solver PyCLES (Pressel et al. 2015). Subgrid-scale fluxes are treated implicitly by the WENO scheme used in the numerical discretization of the equations (Pressel et al. 2017).

For each case, the characteristic timescale of convection is evaluated and taken to be representative of the dynamical decorrelation time τ. Snapshots are taken at least one dynamical decorrelation time apart, so that the cloud samples can be treated as independent in a statistical analysis of the flux biases. The decorrelation timescale is calculated as

$$\tau = \frac{z_{bl}}{w^*} + \frac{d_c}{\bar{w}_u}, \tag{A1}$$

where z_{bl} is the mixed-layer height, $w^* = \left(z_{bl} \, \overline{w'b'}\Big|_s \right)^{1/3}$ is the Deardoff convective velocity, d_c is the cloud depth, and $\bar{w}_u$ is the mean updraft velocity within the cloud.

a. Shallow cumulus (ShCu) convection, BOMEX

The BOMEX LES case study is described in Siebesma et al. (2003). Surface boundary conditions, $\overline{w'q_t'}|_s$ and $\overline{w'\theta_l'}|_s$ are prescribed, resulting in sensible and latent heat fluxes of about 10 and 130 W m^{-2}, respectively. The atmospheric column is forced by clear-sky longwave radiative cooling, neglecting radiative cloud effects. A prescribed subsidence profile induces mean vertical advection of all fields, and specific humidity is further forced by large-scale horizontal advective drying in the lower 500 m. The liquid-water specific humidity is diagnosed through a saturation adjustment procedure. For BOMEX, the characteristic timescale of convection is $\tau \approx 40$ min, where $z_{bl} = 500$ m, $w^* = 0.66$ m s^{-1}, $d_c = 1300$ m, and $\bar{w}_u = 0.85$ m s^{-1}, and snapshots are taken every 1 hour. The domain size is set to 6.4 km in the horizontal and 3 km in the vertical. Results are reported for an isotropic resolution of $\Delta x_i = 20$ m.

b. Shallow cumulus (ShCu) convection, RICO

The RICO LES case study is described in vanZanten et al. (2011). The surface sensible and latent heat fluxes are modeled using bulk aerodynamic formulae with drag coefficients as specified in vanZanten et al. (2011), resulting in fluxes of around 6 and 145 W m^{-2}, respectively. The atmospheric column is forced by prescribed profiles for subsidence and large-scale heat and moisture forcings that are a combination of radiative and advective forcings. The two-moment cloud microphysics scheme from Seifert and Beheng (2006) is used with cloud droplet concentration set to $N_d = 70$ cm^{-3}. For RICO, the characteristic timescale of convection is $\tau \approx 50$ min, where $z_{bl} \approx 500$ m, $w^* \approx 0.62$ m s^{-1}, $d_c = 2500$ m, and $\bar{w}_u \approx 1.2$ m s^{-1}, and snapshots are taken every 1 hour. The domain size is set to 12.8 km in the horizontal and 6 km in the vertical. Results are reported for an isotropic resolution of $\Delta x_i = 40$ m.

c. Stratocumulus-topped marine boundary layer (Sc), DYCOMS-II RF01

The simulation setup for DYCOMS-II RF01 follows the configuration of Stevens et al. (2005). The initial state consists of a well-mixed layer topped by a strong inversion in temperature and specific humidity, with $\Delta\theta_l = 8.5$ K and $\Delta q_t = -7.5$ g kg^{-1}. Surface latent and sensible heat fluxes are prescribed as 115 and 15 W m^{-2}, respectively. In addition, the humidity profile induces radiative cooling above cloud-top and warming at cloud-base. As in BOMEX, the liquid-water specific humidity is diagnosed through a saturation adjustment procedure. For the stratocumulus clouds, without strong updrafts and a thin cloud layer, the characteristic convective timescale is taken to be just the first term of Eq. (A1), which evaluates to $\tau \approx 20$ min, with $z_{bl} = 850$ m and $w^* = 0.8$ m s^{-1}. Snapshots taken every 30 minutes are used in the analysis. The domain size is set to 3.36 km in the horizontal and 1.5 km in the vertical. Results are reported for a resolution of $\Delta z = 5$ m in the vertical and $\Delta x = 35$ m in the horizontal.

d. Deep convection (Cb), TRMM-LBA

Deep convective clouds are generated using the TRMM-LBA configuration detailed in Grabowski et al. (2006), based on observations of the diurnal cycle of convection in the Amazon during the rainy season. The diurnal cycle is forced by the surface fluxes, which are prescribed as a function of time. The magnitude of the fluxes maximizes 5.25 hours after dawn, with a peak latent and sensible heat fluxes of 554 and 270 W m^{-2}, respectively. The radiative cooling profile is also prescribed as a function of time. We use the one-moment microphysics scheme based on Kaul et al. (2015) with modifications described in Shen et al. (2020). Since this case study is not configured to reach a steady state, the simulation is run up to $t = 7$ hours. Deep convection is considered to be fully developed after 5 hours, when the liquid-water and ice-water paths stabilize (Grabowski et al. 2006). The ensemble of cloud snapshots is formed by sampling after $t = 4$, 5.5, and 7 hours from a set of simulations with different initial conditions. For the idealized case (Figs. 1 and 4) only the 15 snapshots from $t = 7$ hours are used. The characteristic convective timescale is given by just the second term of Eq. (A1), $\tau = \int_0^{z_{ct}} \frac{dz}{w_u} \approx 80$ min, where z_{ct} and w_u are the cloud-top height and updraft vertical velocity averaged over the last two hours, respectively. The random perturbations used in the initialization ensure that all cloud snapshots in the ensemble are uncorrelated. The domain size is set to 20 km in the horizontal and 22 km in the vertical. Results are reported for a resolution of $\Delta z = 50$ m in the vertical and $\Delta x = 100$ m in the horizontal.

For the large-domain simulations, we double the domain-size to 40 km in the horizontal and run a smaller ensemble of $N_{\mathrm{LES}} = 5$ simulations. The mean cloud cover, cloud top heights, and cloud water path in the large and small domain ensembles are comparable at 0.30 and 0.32, 11.2 and 9.4 km, and 0.11 and 0.09 g m^{-2}, respectively. The large-domain simulations show a higher degree of aggregation as measured by the variance in total precipitable water, 4.3 mm^2, compared to 3.7 mm^2 in the original 20 km domain. Fig. A1 shows histograms of the total precipitable water for each of the TRMM-LBA simulations at 7 hours ($N_{\mathrm{LES}} = 15$ for the 20 km domain, and $N_{\mathrm{LES}} = 5$ for the 40 km domain). The wider histograms for the large-domain simulations illustrate the larger variance in this field, which is indicative of a higher degree of convective aggregation.

APPENDIX B

Radiative transfer details

We use the libRadtran MYSTIC Monte Carlo solver for the 3D and ICA radiative transfer calculations. The MYSTIC radiative transfer calculations are done using $n = 10^4$ photons sampled from the `kato2` correlated-k parameterization of the solar spectrum (Kato et al. 1999; Mayer and Kylling 2005). The Monte Carlo error scales as $\frac{1}{\sqrt{n}}$, so is on the order of 1%. The surface albedo was set to $\alpha_s = 0.06$ for all RT calculations. The observed surface albedo is accounted for through the scaling described in the main text.

The MYSTIC solver from libRadtran requires 3D fields of liquid and ice water content and particle effective radius as input. The LES uses bulk microphysics schemes and does not explicitly compute the effective radius. For liquid-only clouds, the parameterization from Ackerman et al. (2009) and Blossey et al. (2013) with assumed droplet number of $N_d = 10^8$ m^{-3} is used. The full Mie scattering phase function is taken from the libRadtran lookup tables. Because the lookup tables are only valid for droplets with radius greater than 1 μm, smaller calculated effective radii were rounded to this minimum value.

For ice clouds, the parameterization from Wyser (1998) is used. The `hey` parameterization from Yang et al. (2013) and Emde et al. (2016) with habit type set to `ghm` (general habit mixture) is used. The `hey` parameterization uses the full Mie phase function and does not employ the Henyey-Greenstein approximation, which has been shown to be another source of error in RT (Barker et al. 2015). The results are not dependent on the exact choice for ice crystal shape or roughness (Fig. B1). Note that the `hey` ice parameterization is only valid for radii less than 90 μm, and larger calculated effective radii were rounded to this maximum value.

Deep convective clouds, reaching upwards of 10 km, nearly always contain ice crystals in addition to liquid water. Optical properties of ice crystals depend on their size, shape (or habit), and surface smoothness. Two different parameterizations, with three and four habit choices, respectively, were tested. The differences between these parameterization variants are negligible; they are much smaller than the variability stemming from the cloud dynamics (statistical spread between snapshots) and also much smaller than the magnitude of the 3D effects (Fig. B1).

The `hey` parameterization with general habit mixture (`ghm`) is used in the main text (Yang et al. 2013; Emde et al. 2016). This parameterization is valid for a spectral range from $0.2 - 5\mu$m, and for ice effective radii from $5 - 90\mu$m. `hey` assumes smooth crystals and allows for four choices of habit: `ghm`, solid column (`col`), rough aggregate (`agg`), and `plate`.

The other parameterization tested was `baum_v36` (Heymsfield et al. 2013; Yang et al. 2013; Baum et al. 2014). This parameterization is valid over a wider spectral range ($0.2 - 99\mu$m), but a narrower effective radius range ($5 - 60\mu$m). Particles with effective radius outside of the accepted range were rounded to the maximum allowed value. The `baum_v36` parameterization assumes severely roughened particles. It allows for three choices of habit: `ghm`, solid column (`col`), and rough-aggregate (`agg`).

These seven variants are compared in Fig. B1 for one cloud snapshot from the TRMM-LBA case and they show very similar results. Shown is the TOA reflected flux bias across zenith angles.

Also shown in Fig. B1 is a RT calculation done on the same cloud field, but only including the liquid droplets and ignoring the ice particles. We use the full Mie scattering phase function without any parameterization for the liquid portion of the cloud in all cases. The difference between the liquid-only and liquid + ice TOA fluxes can be up to 20% depending on the parameterization used, but the flux bias (ICA - 3D) is very similar for the liquid-only and all ice parameterizations.

APPENDIX C

Estimating the global flux bias using observations of cloud climatology

a. Cloud property proxy for flux bias

We explored several different cloud properties to use as a proxy for the flux bias. Our limited study concluded that the cloud top height (CTH) was the best proxy because it shows a strong positive, linear correlation with flux bias. Other cloud scene properties we examined included cloud depth, cloud cover (cc), and the geometric mean of covered area and uncovered area, $\sqrt{\mathrm{cc}(1-\mathrm{cc})}$. The linear regression fits are shown in Fig. C1 for the sun at zenith. The RMS error for CTH is the smallest. Although cloud depth is also a reasonable proxy, and possibly more physical, it is more difficult to measure from satellite, and therefore we use CTH in this study. An important extension to this work would be to allow for multiple cloud properties and a more complex model than a linear fit to describe the flux bias. However, with our limited data from only four LES cases in this present study, we do not feel justified to use a more complex model.

b. Surface albedo correction

As described in the main text, we make a correction to account for the observed surface albedo using Eq. 5 when estimating the global flux bias. This correction is derived by assuming multiple-scattering within the cloudy scene can be ignored and that the baseline surface and cloud albedos are independent of zenith angle. Justification for these assumptions is demonstrated in Fig. C2 by the good agreement between the computed albedo bias and the predicted albedo bias.

References

Ackerman, A. S., and Coauthors, 2009: Large-eddy simulations of a drizzling, stratocumulus-topped marine boundary layer. *Monthly Weather Review*, **137 (3)**, 1083–1110, doi:10.1175/2008MWR2582.1.

Barker, H. W., J. N. S. Cole, J. Li, B. Yi, and P. Yang, 2015: Estimation of Errors in Two-Stream Approximations of the Solar Radiative Transfer Equation for Cloudy-Sky Conditions. *Journal of the Atmospheric Sciences*, **72 (11)**, 4053–4074, doi:10.1175/JAS-D-15-0033.1.

Barker, H. W., S. Kato, and T. Wehr, 2012: Computation of solar radiative fluxes by 1D and 3D methods using cloudy atmospheres inferred from A-train satellite data. *Surveys in Geophysics*, **33 (3-4)**, 657–676, doi:10.1007/s10712-011-9164-9.

Barker, H. W., and Coauthors, 2003: Assessing 1D Atmospheric Solar Radiative Transfer Models: Interpretation and Handling of Unresolved Clouds. *Journal of Climate*, **16 (16)**, 2676–2699, doi:10.1175/1520-0442(2003)016<2676:ADASRT>2.0.CO;2.

Baum, B. A., P. Yang, A. J. Heymsfield, A. Bansemer, B. H. Cole, A. Merrelli, C. Schmitt, and C. Wang, 2014: Ice cloud single-scattering property models with the full phase matrix at wavelengths from 0.2 to 100um. *Journal of Quantitative Spectroscopy and Radiative Transfer*, **146**, 123–139, doi:10.1016/j.jqsrt.2014.02.029.

Bender, F. A.-M., H. Rodhe, R. J. Charlson, A. M. L. Ekman, and N. Loeb, 2006: 22 views of the global albedo—comparison between 20 GCMs and two satellites. *Tellus A: Dynamic Meteorology and Oceanography*, **58 (3)**, 320–330, doi:10.1111/j.1600-0870.2006.00181.x.

Blossey, P. N., and Coauthors, 2013: Marine low cloud sensitivity to an idealized climate change: The CGILS LES intercomparison. *Journal of Advances in Modeling Earth Systems*, **5 (2)**, 234–258, doi:10.1002/jame.20025.

Cahalan, R., and W. Wiscombe, 1992: Proceedings of the Second Atmospheric Radiation Measurement (ARM) Science Team Meeting. *Plane-Parallel Albedo Bias*, Denver, Colorado, 35, December.

Cahalan, R. F., W. Ridgway, W. J. Wiscombe, S. Gollmer, and Harshvardhan, 1994: Independent Pixel and Monte Carlo Estimates of Stratocumulus Albedo. *Journal of the Atmospheric Sciences*, **51 (24)**, 3776–3790, doi:10.1175/1520-0469(1994)051<3776:IPAMCE>2.0.CO;2.

Cohen, Y., I. Lopez-Gomez, A. Jaruga, J. He, C. M. Kaul, and T. Schneider, 2020: Unified entrainment and detrainment closures for extended eddy-diffusivity mass-flux schemes. *Journal of Advances in Modeling Earth Systems*, doi:10.1029/2020MS002162.

Cole, J. N. S., H. W. Barker, W. O'Hirok, E. E. Clothiaux, M. F. Khairoutdinov, and D. A. Randall, 2005: Atmospheric radiative transfer through global arrays of 2D clouds. *Geophysical Research Letters*, **32 (19)**, doi:10.1029/2005GL023329.

Emde, C., and Coauthors, 2016: The libRadtran software package for radiative transfer calculations (version 2.0.1). *Geoscientific Model Development*, **9 (5)**, 1647–1672, doi:10.5194/gmd-9-1647-2016.

Engström, A., F. A.-M. Bender, R. J. Charlson, and R. Wood, 2015: The nonlinear relationship between albedo and cloud fraction on near-global, monthly mean scale in observations and in the cmip5 model ensemble. *Geophysical Research Letters*, **42 (21)**, 9571–9578, doi:https://doi.org/10.1002/2015GL066275.

Frame, J. W., J. L. Petters, P. M. Markowski, and J. Y. Harrington, 2009: An application of the tilted independent pixel approximation to cumulonimbus environments. *Atmospheric Research*, **91**, 127–136, doi:10.1016/j.atmosres.2008.05.005.

Grabowski, W. W., and Coauthors, 2006: Daytime convective development over land: A model intercomparison based on LBA observations. *Quarterly Journal of the Royal Meteorological Society*, **132 (615)**, 317–344, doi:10.1256/qj.04.147.

Gristey, J. J., and Coauthors, 2019: Surface solar irradiance in continental shallow cumulus fields: Observations and large eddy simulation. *Journal of the Atmospheric Sciences*, 19–0261, doi:10.1175/JAS-D-19-0261.1.

Heymsfield, A. J., C. Schmitt, A. Bansemer, A. J. Heymsfield, C. Schmitt, and A. Bansemer, 2013: Ice cloud particle size distributions and pressure-dependent terminal velocities from in situ observations at temperatures from 0° to -86°C. *Journal of the Atmospheric Sciences*, **70 (12)**, 4123–4154, doi:10.1175/JAS-D-12-0124.1.

Hogan, R. J., and A. Bozzo, 2018: A flexible and efficient radiation scheme for the ecmwf model. *Journal of Advances in Modeling Earth Systems*, **10**, 1990–2008, doi:https://doi.org/10.1029/2018MS001364, https://doi.org/10.1029/2018MS001364.

Hogan, R. J., M. D. Fielding, H. W. Barker, N. Villefranque, and S. A. K. Schäfer, 2019: Entrapment: An important mechanism to explain the shortwave 3d radiative effect of clouds. *Journal of the Atmospheric Sciences*, **2019**, 48–66, doi:10.1175/JAS-D-18-0366.1.

Hogan, R. J., and J. K. P. Shonk, 2013: Incorporating the Effects of 3D Radiative Transfer in the Presence of Clouds into Two-Stream Multilayer Radiation Schemes. *Journal of the Atmospheric Sciences*, **70 (2)**, 708–724, doi:10.1175/JAS-D-12-041.1.

Hourdin, F., and Coauthors, 2020: LMDZ6A: the atmospheric component of the IPSL climate model with improved and better tuned physics. *Journal of Advances in Modeling Earth Systems*, doi:10.1029/2019MS001892.

Jeevanjee, N., and D. M. Romps, 2013: Convective self-aggregation, cold pools, and domain size. *Geophysical Research Letters*, **40 (5)**, 994–998, doi:10.1002/grl.50204.

Kato, S., T. P. Ackerman, J. H. Mather, and E. E. Clothiaux, 1999: The k-distribution method and correlated-k approximation for a shortwave radiative transfer model. *Journal of Quantitative Spectroscopy and Radiative Transfer*, **62 (1)**, 109 – 121, doi:https://doi.org/10.1016/S0022-4073(98)00075-2.

Kaul, C. M., J. Teixeira, and K. Suzuki, 2015: Sensitivities in Large-Eddy Simulations of Mixed-Phase Arctic Stratocumulus Clouds Using a Simple Microphysics Approach. *Monthly Weather Review*, **143 (11)**, 4393–4421, doi:10.1175/MWR-D-14-00319.1.

Khairoutdinov, M. F., and D. A. Randall, 2001: A cloud resolving model as a cloud parameterization in the NCAR Community Climate System Model: Preliminary results. *Geophysical Research Letters*, **28 (18)**, 3617–3620, doi:10.1029/2001GL013552.

Kooperman, G. J., M. S. Pritchard, M. A. Burt, M. D. Branson, and D. A. Randall, 2016: Robust effects of cloud superparameterization on simulated daily rainfall intensity statistics across multiple versions of the Community Earth System Model. *Journal of Advances in Modeling Earth Systems*, **8 (1)**, 140–165, doi:10.1002/2015MS000574.

Marchand, R., T. Ackerman, M. Smyth, and W. B. Rossow, 2010: A review of cloud top height and optical depth histograms from MISR, ISCCP, and MODIS. *Journal of Geophysical Research*, **115 (D16)**, doi:10.1029/2009JD013422.

Marshak, A., and A. Davis, Eds., 2005: *3D radiative transfer in cloudy atmospheres*. Physics of Earth and Space Environments, Springer-Verlag, Berlin/Heidelberg, doi:10.1007/3-540-28519-9.

Marshak, A., A. Davis, W. Wiscombe, and R. Cahalan, 1995a: Radiative smoothing in fractal clouds. *Journal of Geophysical Research*, **100 (D12)**, 26 247, doi:10.1029/95JD02895.

Marshak, A., A. Davis, W. Wiscombe, and G. Titov, 1995b: The verisimilitude of the independent pixel approximation used in cloud remote sensing. *Remote Sensing of Environment*, **52**, 71–78, doi:10.1016/0034-4257(95)00016-T.

Mayer, B., 2009: Radiative transfer in the cloudy atmosphere. *EPJ Web of Conferences*, **1**, 75–99, doi:10.1140/epjconf/e2009-00912-1.

Mayer, B., and A. Kylling, 2005: Technical note: The libRadtran software package for radiative transfer calculations - description and examples of use. *Atmospheric Chemistry and Physics*, **5 (7)**, 1855–1877, doi:10.5194/acp-5-1855-2005.

Myhre, G., and Coauthors, 2013: Anthropogenic and Natural Radiative Forcing. *Climate Change 2013: The Physical Science Basis. Contribution of Working Group I to the Fifth Assessment Report of the Intergovernmental Panel on Climate Change*, T. Stocker, D. Qin, G.-K. Plattner, M. Tignor, S. Allen, J. Boschung, A. Nauels, Y. Xia, V. Bex, and P. Midgley, Eds., Cambridge University Press, Cambridge, United Kingdom and New York, NY, USA, chap. 8, 659–740.

Okata, M., T. Nakajima, K. Suzuki, T. Inoue, T. Y. Nakajima, and H. Okamoto, 2017: A study on radiative transfer effects in 3-D cloudy atmosphere using satellite data. *Journal of Geophysical Research: Atmospheres*, **122 (1)**, 443–468, doi:10.1002/2016JD025441.

Patrizio, C. R., and D. A. Randall, 2019: Sensitivity of Convective Self-Aggregation to Domain Size. *Journal of Advances in Modeling Earth Systems*, **11 (7)**, 1995–2019, doi: 10.1029/2019MS001672.

Pincus, R., H. W. Barker, and J.-J. Morcrette, 2003: A fast, flexible, approximate technique for computing radiative transfer in inhomogeneous cloud fields. *Journal* *of Geophysical Research: Atmospheres*, **108**, doi:https://doi.org/10.1029/2002JD003322, https://doi.org/10.1029/2002JD003322.

Pressel, K. G., C. M. Kaul, T. Schneider, Z. Tan, and S. Mishra, 2015: Large-eddy simulation in an anelastic framework with closed water and entropy balances. *Journal of Advances in Modeling Earth Systems*, **7 (3)**, 1425–1456, doi:10.1002/2015MS000496.

Pressel, K. G., S. Mishra, T. Schneider, C. M. Kaul, and Z. Tan, 2017: Numerics and subgrid-scale modeling in large eddy simulations of stratocumulus clouds. *Journal of Advances in Modeling Earth Systems*, **9 (2)**, 1342–1365, doi:10.1002/2016MS000778.

Rossow, W., and E. Duenas, 2004: The International Satellite Cloud Climatology Project (ISCCP) web site: An online resource for research. *Bulletin of the American Meteorological Society*, **85 (2)**, 167–176, doi:10.1175/BAMS-85-2-167.

Rossow, W. B., R. A. Schiffer, W. B. Rossow, and R. A. Schiffer, 1999: Advances in understanding clouds from ISCCP. *Bulletin of the American Meteorological Society*, **80 (11)**, 2261–2287, doi:10.1175/1520-0477(1999)080<2261:AIUCFI>2.0.CO;2.

Schäfer, S. A. K., R. J. Hogan, C. Klinger, J. C. Chiu, and B. Mayer, 2016: Representing 3-D cloud radiation effects in two-stream schemes: 1. Longwave considerations and effective cloud edge length. *Journal of Geophysical Research: Atmospheres*, **121 (14)**, 8567–8582, doi:10.1002/2016JD024876.

Schneider, T., J. Teixeira, C. S. Bretherton, F. Brient, K. G. Pressel, C. Schär, and A. P. Siebesma, 2017: Climate goals and computing the future of clouds. *Nature Climate Change opinion & comment*, **7 (1)**, 3–5, doi:10.1038/nclimate3190.

Seifert, A., and K. D. Beheng, 2006: A two-moment cloud microphysics parameterization for mixed-phase clouds. Part 1: Model description. *Meteorology and Atmospheric Physics*, **92 (1-2)**, 45–66, doi:10.1007/s00703-005-0112-4.

Shen, Z., K. G. Pressel, Z. Tan, and T. Schneider, 2020: Statistically Steady State Large-Eddy Simulations Forced by an Idealized GCM: 1. Forcing Framework and Simulation Characteristics. *Journal of Advances in Modeling Earth Systems*, **12 (2)**, doi:10.1029/2019MS001814.

Shonk, J. K. P., and R. J. Hogan, 2008: Tripleclouds: An efficient method for representing horizontal cloud inhomogeneity in 1d radiation schemes by using three regions at each height. *Journal of Climate*, **21**, 2352–2370, doi:10.1175/2007JCLI1940.1.

Siebesma, A. P., and Coauthors, 2003: A large eddy simulation intercomparison study of shallow cumulus convection. *Journal of the Atmospheric Sciences*, **60 (10)**, 1201–1219, doi:10.1175/1520-0469(2003)60<1201:ALESIS>2.0.CO;2.

Singer, C., I. Lopez-Gomez, X. Zhang, and T. Schneider, 2020: Data for “Top-of-atmosphere albedo bias from neglecting three-dimensional radiative transfer through clouds”. CaltechDATA, doi:10.22002/D1.1637.

Stephens, G. L., D. O’Brien, P. J. Webster, P. Pilewski, S. Kato, and J.-l. Li, 2015: The albedo of Earth. *Reviews of Geophysics*, **53 (1)**, 141–163, doi:10.1002/2014RG000449.

Stevens, B., and Coauthors, 2005: Evaluation of large-eddy simulations via observations of nocturnal marine stratocumulus. *Monthly Weather Review*, **133 (6)**, 1443–1462, doi:10.1175/MWR2930.1.

Stubenrauch, C., W. Rossow, and S. Kinne, 2012: Assessment of global cloud data sets from satellites: A project of the world climate research programme Global Energy and Water Cycle Experiment (GEWEX) Radiation Panel. Tech. Rep. 23, World Climate Research Programme.

Stubenrauch, C. J., and Coauthors, 2013: Assessment of clobal cloud datasets from satellites: Project and database initiated by the GEWEX radiation panel. *Bulletin of the American Meteorological Society*, **94 (7)**, 1031–1049, doi:10.1175/BAMS-D-12-00117.1.

vanZanten, M. C., and Coauthors, 2011: Controls on precipitation and cloudiness in simulations of trade-wind cumulus as observed during RICO. *Journal of Advances in Modeling Earth Systems*, **3 (2)**, doi:10.1029/2011MS000056.

Várnai, T., and R. Davies, 1999: Effects of cloud heterogeneities on shortwave radiation: Comparison of cloud-top variability and internal heterogeneity. *Journal of the Atmospheric Sciences*, **56 (24)**, 4206–4224, doi:10.1175/1520-0469(1999)056<4206:EOCHOS>2.0.CO;2.

Veerman, M. A., X. Pedruzo-Bagazgoitia, F. Jakub, J. Vilà-Guerau de Arellano, and C. C. Heerwaarden, 2020: Three-Dimensional Radiative Effects By Shallow Cumulus Clouds on Dynamic Heterogeneities Over a Vegetated Surface. *Journal of Advances in Modeling Earth Systems*, **12 (7)**, doi:10.1029/2019MS001990.

Villefranque, N., R. Fournier, F. Couvreux, S. Blanco, C. Cornet, V. Eymet, V. Forest, and J. Tregan, 2019: A Path-Tracing Monte Carlo Library for 3-D Radiative Transfer in Highly Resolved Cloudy Atmospheres. *Journal of Advances in Modeling Earth Systems*, **11 (8)**, 2449–2473, doi:10.1029/2018MS001602, 1902.01137.

Voigt, A., B. Stevens, J. Bader, and T. Mauritsen, 2013: The observed hemispheric symmetry in reflected shortwave irradiance. *J. Climate*, **26**, 468–477, doi:https://doi.org/10.1175/

JCLI-D-12-00132.1.

Wing, A. A., K. Emanuel, C. E. Holloway, and C. Muller, 2017: Convective Self-Aggregation in Numerical Simulations: A Review. *Surveys in Geophysics*, **38 (6)**, 1173–1197, doi:10.1007/s10712-017-9408-4.

Wissmeier, U., R. Buras, and B. Mayer, 2013: paNTICA: A fast 3D radiative transfer scheme to calculate surface solar irradiance for NWP and LES models. *Journal of Applied Meteorology and Climatology*, **52 (8)**, 1698–1715, doi:10.1175/JAMC-D-12-0227.1.

Wyser, K., 1998: The effective radius in ice clouds. *Journal of Climate*, **11 (7)**, 1793–1802, doi:10.1175/1520-0442(1998)011<1793:TERIIC>2.0.CO;2.

Yang, P., and Coauthors, 2013: Spectrally consistent scattering, absorption, and polarization properties of atmospheric ice crystals at wavelengths from 0.2 to 100 um. *Journal of the Atmospheric Sciences*, **70 (1)**, 330–347, doi:10.1175/JAS-D-12-039.1.

Zhao, M., and Coauthors, 2018: The GFDL Global Atmosphere and Land Model AM4.0/LM4.0: 2. Model Description, Sensitivity Studies, and Tuning Strategies. *Journal of Advances in Modeling Earth Systems*, **10 (3)**, 735–769, doi:10.1002/2017MS001209.

LIST OF FIGURES

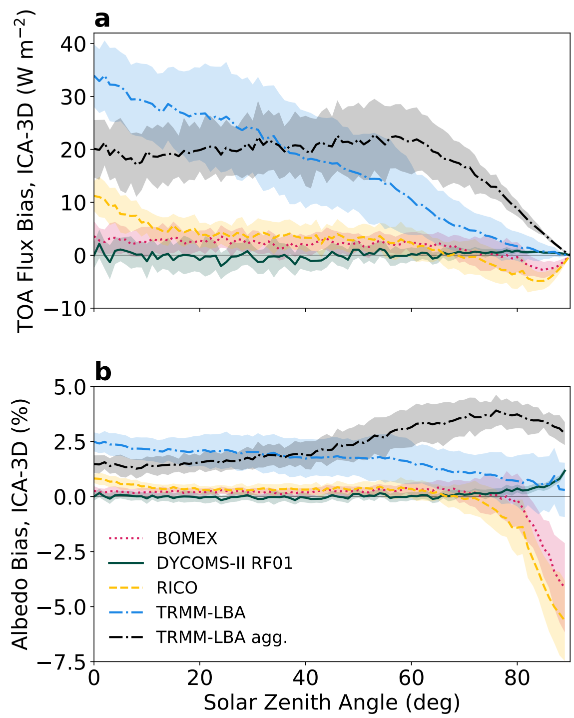

768 FIG. 1. Bias (ICA-3D) in (a) TOA reflected flux and (b) albedo as a function of zenith angle for ShCu (BOMEX
769 and RICO), Sc (DYCOMS-II RF01), and Cb (TRMM-LBA and TRMM-LBA agg.). For each cloud type, average
770 fluxes (with shaded 1σ error bars) are computed over the individual snapshots. Positive bias means the ICA
771 approximation is reflecting more incoming flux than in the 3D RT calculation.

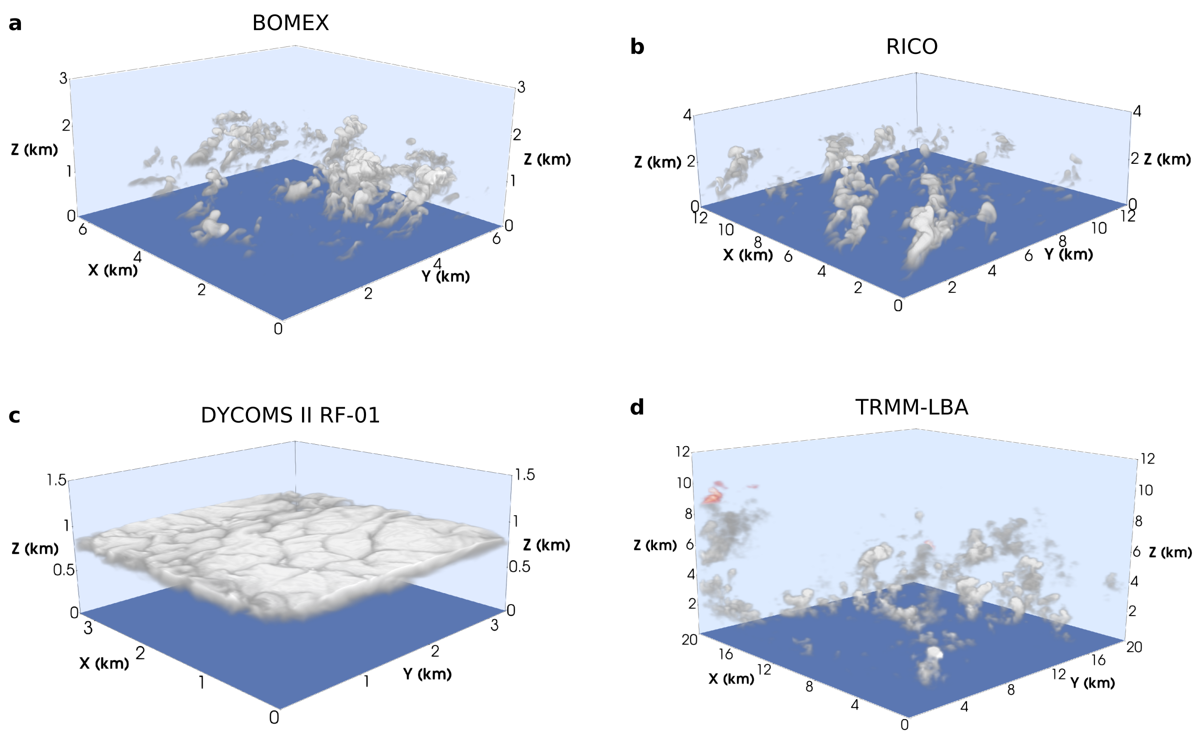

FIG. 2. Snapshots of LES clouds, showing liquid water specific humidity (gray to white, low to high) and ice water specific humidity (red to white, low to high). (a) and (b) Shallow convective clouds. (c) Stratocumulus clouds. (d) Deep convective clouds. Note that the domain sizes vary between the cases. At high zenith angles, cloud shadowing becomes important for ShCu because the individual clouds can shadow a large portion of the domain and scattering from the cloud sides becomes dominant due to the low angle of the incoming photons.

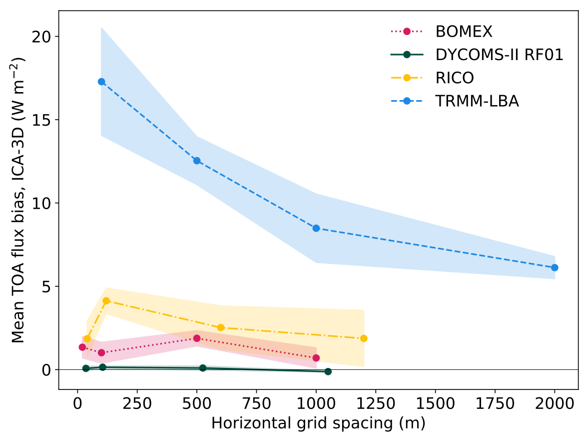

777 FIG. 3. Mean TOA reflected flux bias across all solar zenith angles computed for different resolutions of the
778 same cloud fields. The horizontal axis shows the horizontal resolution; the vertical resolution is kept fixed. The
779 four cases of ShCu, Sc, and Cb are shown in the same colors as Fig. 1. For each case, three snapshots from the
780 original ensemble are used and the spread is shown by the shading.

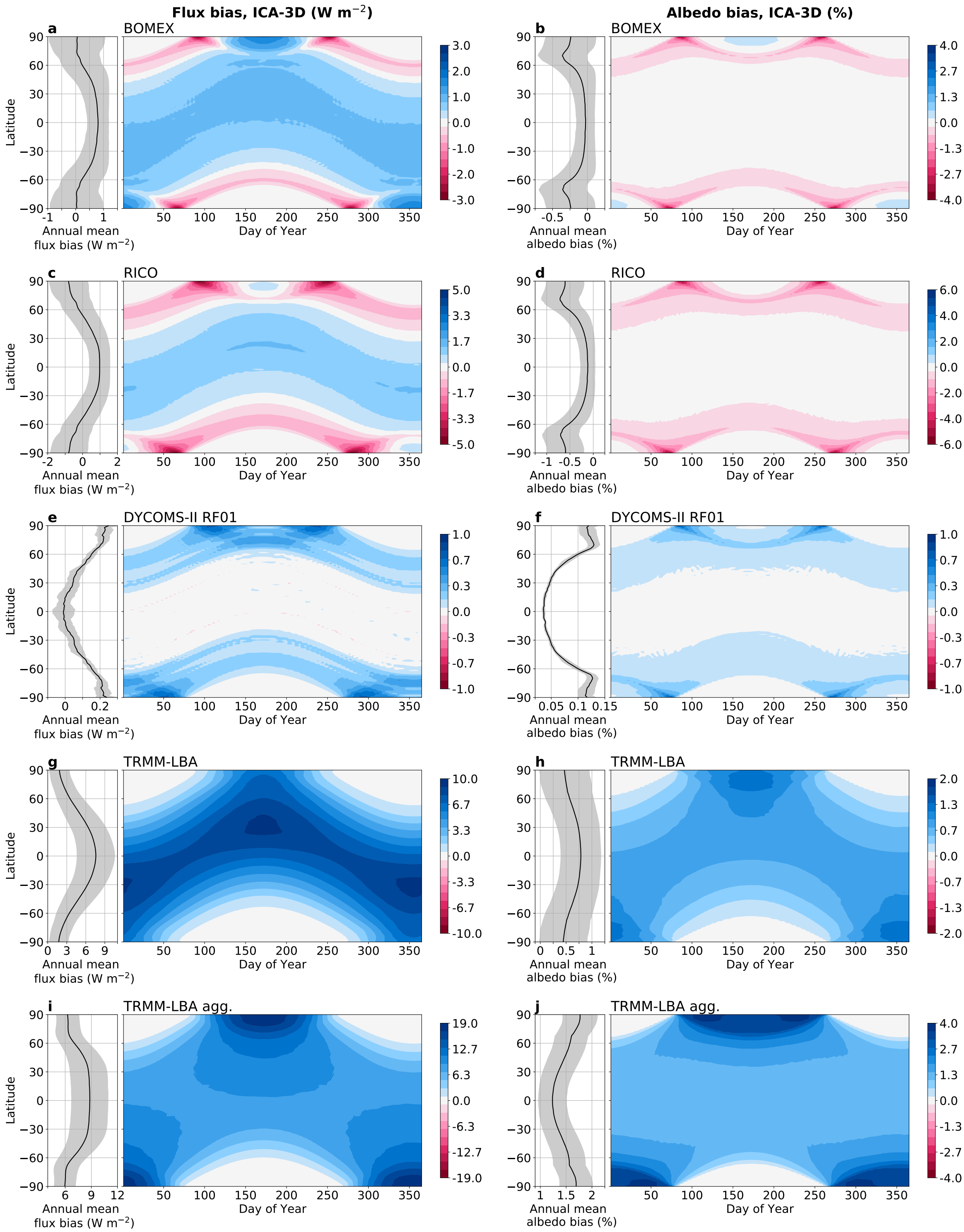

FIG. 4. Daily mean bias (ICA-3D) as a function of latitude and day of year assuming the globe is covered by (a-d) ShCu (BOMEX and RICO), (e-f) Sc (DYCOMS-II RF01), (g-h) Cb (TRMM-LBA), and (i-j) more aggregated Cb (TRMM-LBA agg.). Left column shows flux bias, and right columns shows albedo bias. Note the color scales vary between LES cases. Inset panels on the left show annual average biases with shaded error bars that denote the spread across the LES ensembles as described in the text.

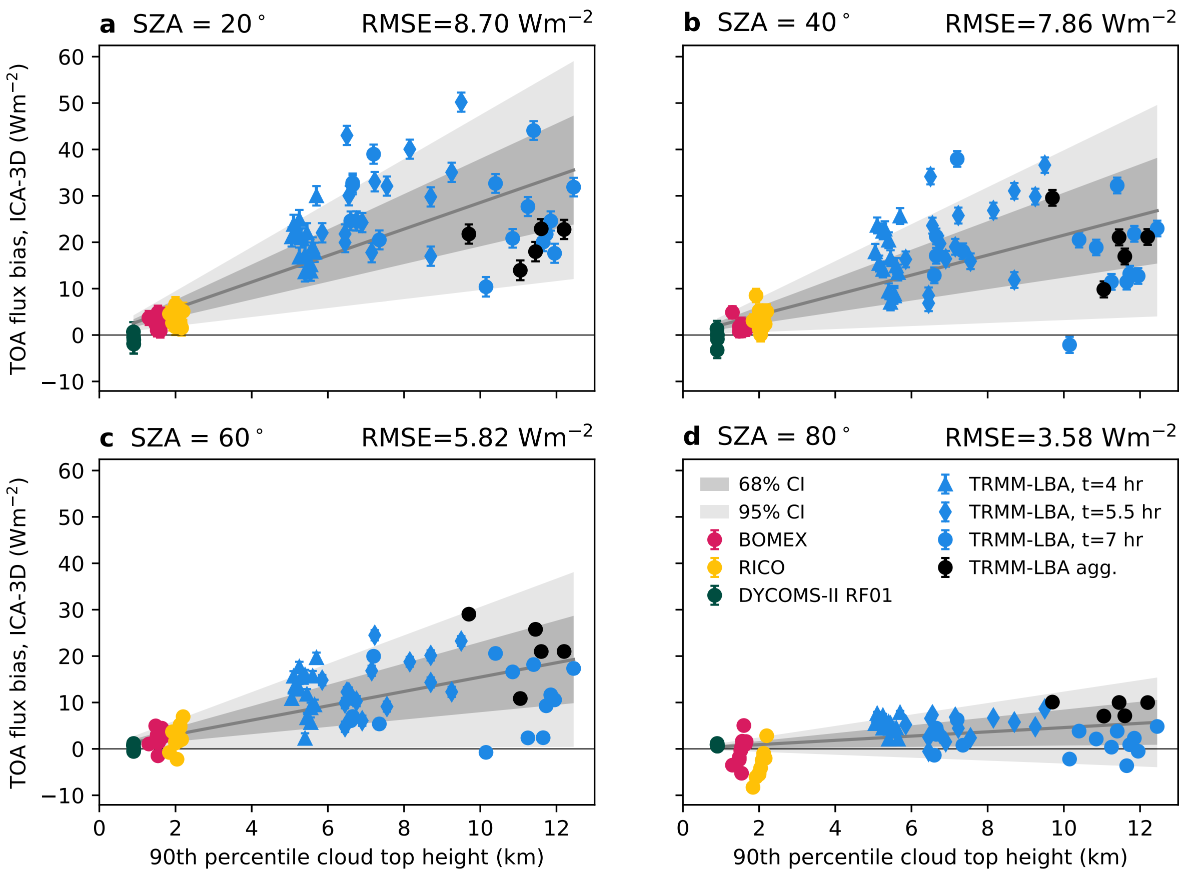

FIG. 5. Scatter plot of 90th percentile cloud top height (CTH) from LES domain against flux bias at zenith angles (a) 20°, (b) 40°, (c) 60°, and (d) 80°. LES ensemble members are plotted with the same color convention as in Fig. 1. The grey lines show the regression fit constrained to go through the origin. The gray shaded areas show the 68% and 95% confidence intervals. The RMS error of the regression is indicated at the top.

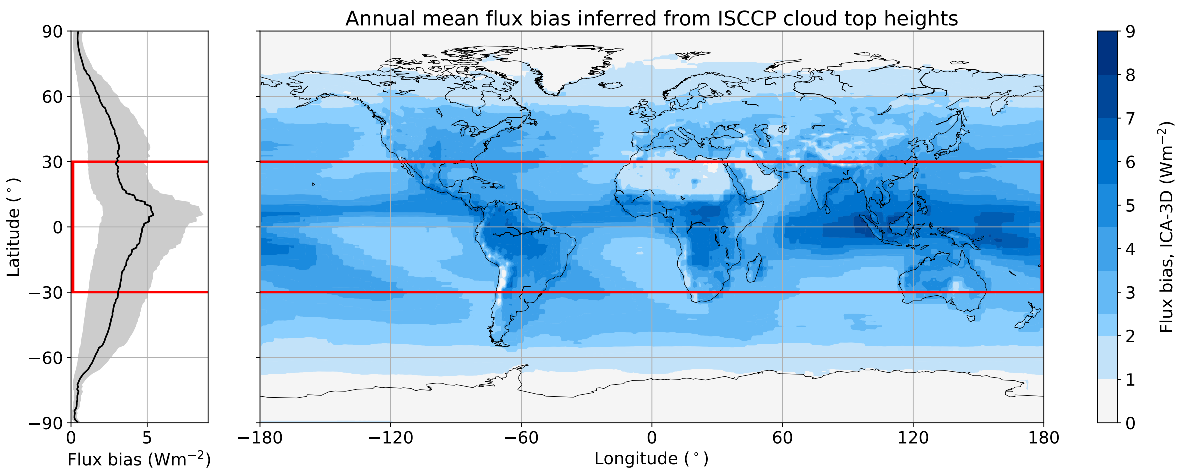

FIG. 6. Map of annual mean flux bias inferred from ISCCP CTH. Left panel shows the zonally-averaged flux bias in the black line and 1σ error bars in the grey shading that are derived from the linear regression in Fig. 5.

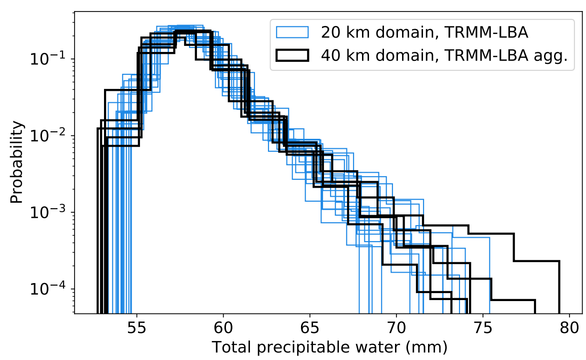

Fig. A1. Normalized histogram of total precipitable water from the TRMM-LBA simulations in a 20 km domain vs. 40 km domain, which we use as a less and more-aggregated case of deep convection. The variance across the ensemble, shown by the width of the histogram, is representative of the degree of convective aggregation.

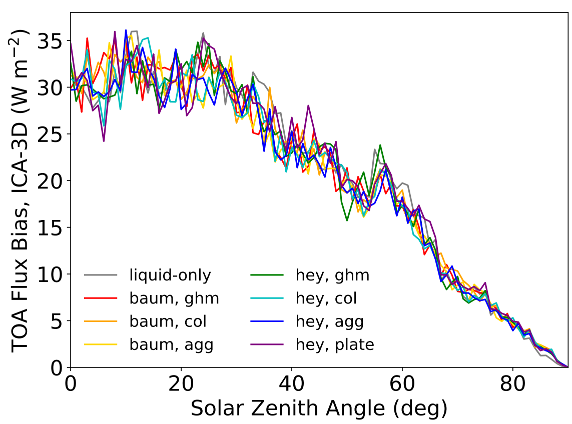

796 Fig. B1. TOA reflected bias across zenith angles for different ice parameterizations in one TRMM-LBA
797 cloud snapshot.

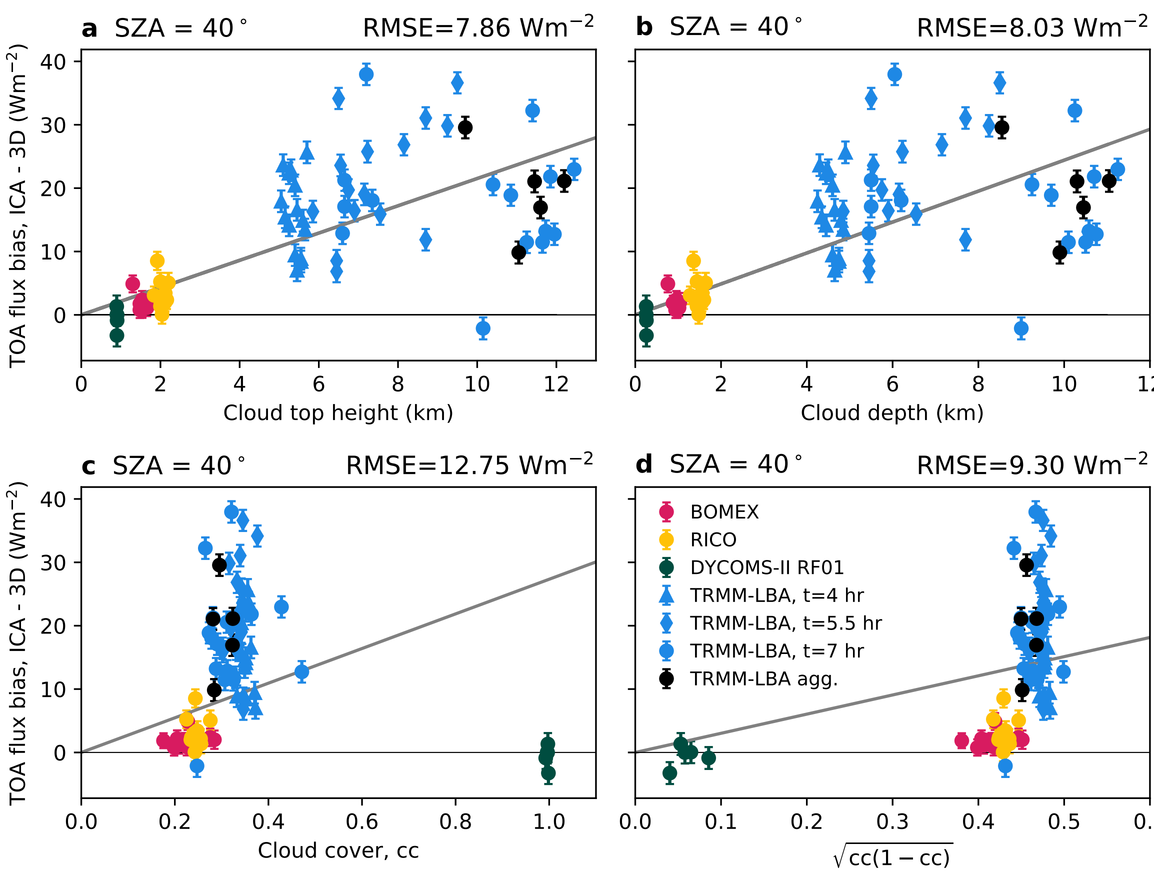

798 Fig. C1. Regression of flux bias on several different cloud properties (a) cloud top height, (b) cloud depth, (c)
799 cloud cover, and (d) $\sqrt{cc(1-cc)}$. All panels show the flux bias for a zenith angle of 40°. (a) is the same as
800 Fig. 5b. The RMS error is shown for each panel and is smallest for the cloud top height case (a).

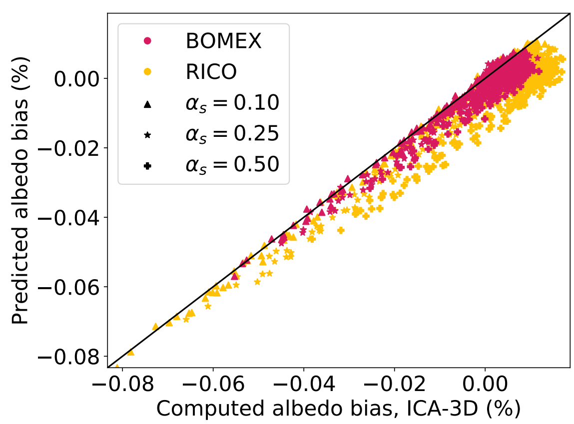

801 Fig. C2. Predicted albedo from Eq. 5 compared to the computed albedo from Monte Carlo RT simulation
802 with different surface albedo α_s in two ShCu cases. The black line shows the 1:1 ratio for reference.